MODE-III FRACTURE TOUGHNESS OF ANTICRACKS IN WEAK LAYERS: MODELLING AND EXPERIMENTS

Florian Rheinschmidt[1,*], Valentin Adam[1,2], Melin Walet[2], Jakob Schöttner[2], Bastian Bergfeld[2], Alec van Herwijnen[2], Philipp Weißgraeber[3], Philipp L. Rosendahl[1]

[1] *Technical University of Darmstadt, Institute of Structural Mechanics and Design, Darmstadt, Germany*
[2] *WSL Institute for Snow and Avalanche Research SLF, Davos Dorf, Switzerland*
[3] *University of Rostock, Chair of Lightweight Design, Rostock, Germany*

ABSTRACT: We propose an experimental setup and a closed-form model to identify the mode III fracture toughness of weak layers. The field experiment draws inspiration from out-of-plane double cantilever beam tests that are used to determine the mode III fracture toughness of adhesives and from classical propagation saw tests. For the calculation of energy release rates, our mechanical model uses the theory of bi-axial bending and torsion of laminate beams on an elastic foundation. These kinematics in combination with the principle of minimum potential energy result in an efficient and accurate description of stresses and energy release rates. Model and experiments distinguish contributions to the total energy release rate from all three fracture modes and, hence, can be used to determine mixed-mode interaction laws for weak layers.

Keywords: fracture mechanics, propagation saw test, cross-slope anticrack propagation

1. INTRODUCTION

Dry-snow slab avalanches originate from mixed-mode cracking of buried weak layers in the stratified snowpack. Porous weak layers of depth hoar or surface hoar are prone to collapse (Schweizer et al. [2003], Heierli and Zaiser [2008]). This so-called anticrack phenomenon makes the release of slab avalanches a fracture mechanics problem. Crack and anticrack propagation are energy-driven processes, where the energy released by crack propagation equals the fracture toughness, i.e., the resistance of the material against crack growth (Griffith [1921]).

Three different fracture modes are distinguished, each associated with an independent fracture toughness: mode I (closing or opening) describes crack surfaces moving toward or away from each other perpendicular to the direction of crack growth, mode II (shearing) describes the in-plane shear movement of crack surfaces against each other in the direction of crack growth, and mode III (tearing) is associated with an out-of-plane shear movement of the crack surfaces. In the context of avalanche triggering, mode I corresponds to weak-layer collapse and is omnipresent on any terrain, mode II is present in downslope or upslope crack propagation and cross-slope propagation is governed by mode III. Recent work tackled mode I-II mixity for persistent weak layers using modified propagation saw tests (Adam et al. [2023]) and a mechanical model of the layered snowpack (Weißgraeber and Rosendahl [2023]). However, the mode III fracture toughness remains unknown.

Numerical studies investigated the propagation of anticracks in weak layers in both slope-parallel and cross-slope direction (Trottet et al. [2022]). Especially anticracks travelling across the slope result in snow slabs that are subject to out-of-plane bending. Here, mode III conditions occur at the anticrack tip in the weak layer. Thus, identifying the mode III fracture toughness is crucial for understanding cross-slope crack propagation.

The classical propagation saw test (PST) is adapted by Adam et al. [2023] to measure mode II fracture toughness. Instead of considering the whole slab, the loading situations are controlled more carefully by reducing the slab thickness and introducing additional surface weights. This allows for controlling the mode ratio between modes I and II. The mechanical model for layered snow slabs resting on an elastic weak layer, proposed by Weißgraeber and Rosendahl [2023], provides the energy release rate at anticrack propagation.

Neither the experimental setup nor the mechanical model are capable of handling mode III conditions. In order to address this deficiency and provide additional mechanical properties of weak layers, a new mechanical model based on the principle of the minimum of the total potential is introduced.

An experiment addressing this knowledge gap is the cross slope propagation saw test (CPST) proposed by Knoff [2014]. Instead of creating a downslope propagation saw test, the PST specimen is dug

*Corresponding author address:
F. Rheinschmidt, Institute of Structural Mechanics and Design
Franziska-Braun-Str. 3, 64287 Darmstadt, Germany
tel: +49 6151 16 23035
mail: rheinschmidt@ismd.tu-darmstadt.de

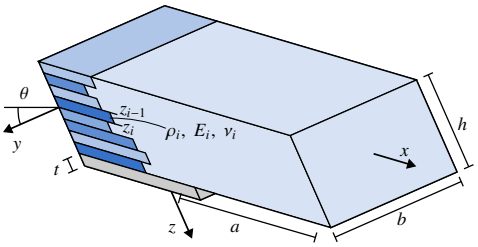

Figure 1: Depiction of the CPST specimen with slab thickness h, slab out-of-plane thickness b, weak layer's thickness t and cut length a. θ is the tilt around the x-axis. The slab's layers are defined by their density ρ_i, mechanical properties E_i and ν_i and thickness $t_i = z_i - z_{i-1}$. Numbering of the layers is done from top to bottom. The weak layer is depicted in grey, the slab is blue.

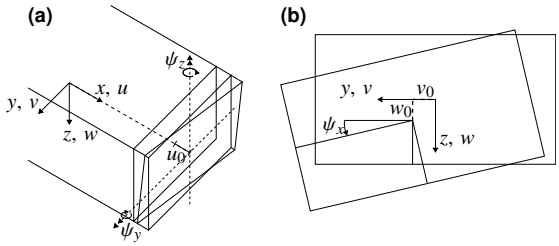

Figure 2: Displacement field of the slab with **(a)** the two rotational degrees of freedom ψ_y and ψ_z, and the centerline displacement u_0 governing the axial displacement u and **(b)** the torsional rotation ψ_x and the two centerline translations v_0 and w_0 governing the out-of-plane and in-plane bending deformations v and w.

in cross slope direction. This results in a reduced effort for large testing series. Measured cut lengths were similar to the ones measured in classical PST-specimen. With the present model, the CPSTs by Knoff are evaluated and a dedicated mode III PST setup is proposed.

2. CLOSED-FORM MODEL FOR OUT-OF-PLANE BENDING

We use the principle of minimum potential energy in combination with the calculus of variations to derive the system of equations governing bi-axial bending (Methfessel and Becker [2022]). For this purpose, the kinematics of the layered snow slab on a weak layer are formulated. Using Hooke's law, strains and stresses are derived. The strain energy can be computed from these quantities. In combination with the external work, conducted by gravity, and additional loads in the form of weights placed on the slab, an expression for the total potential energy on a bedded snow slab is derived. Applying the calculus of variations results in the Euler system, a system of linear ordinary differential equations of second order, that can be solved by standard means.

2.1 Governing equations

The displacement field for the bedded slab, subject to both in-plane and out-of-plane bending is derived from bi-axial Timoshenko kinematics, where the axial displacement u is dependent on the centerline displacement u_0 and the rotations about the horizontal and vertical axis y and z, ψ_y and ψ_z. This aligns with classical Timoshenko kinematics with two rotational degrees of freedom. Additionally, the out-of-plane displacement v and the in-plane bending w are linked by the torsional rotation of the beam ψ_x, that contributes linearly over the in-plane thickness z and the out-of-plane thickness y to the displacements. The kinematics for the axial displacement and the bending displacement are displayed in Figure 2.

The layering depicted in Figure 1 is regarded by Young's modulus and densities of the individual layers. With these kinematics, strains and stresses can be computed and the strain energy density is derived.

2.2 Slabs on weak-layer support

In order to represent both in-plane and out-of-plane deformations of the weak layer, an ansatz with both constant and linear terms in the out-of-plane direction y is chosen for all three displacement components. Additionally, we require the displacement field to be continuous in the interface with the slab and to be vanishing at the lower interface towards the substratum. Through the thickness of the weak layer, both a linear and cosine-shaped form are allowed:

$$
\begin{aligned}
u_{\mathrm{wl}}(x,y,z) &= u\left(x,y,\frac{h}{2}\right)\left(1-\frac{z-h/2}{t}\right) \\
&\quad + \cos\left(\frac{2z-h-t}{2t}\pi\right)\left(\theta_{\mathrm{uc}}+\frac{2y}{b}\theta_{\mathrm{ul}}\right) \\
v_{\mathrm{wl}}(x,y,z) &= v\left(x,y,\frac{h}{2}\right)\left(1-\frac{z-h/2}{t}\right) \\
&\quad + \cos\left(\frac{2z-h-t}{2t}\pi\right)\left(\theta_{\mathrm{vc}}+\frac{2y}{b}\theta_{\mathrm{vl}}\right) \\
w_{\mathrm{wl}}(x,y,z) &= w\left(x,y,\frac{h}{2}\right)\left(1-\frac{z-h/2}{t}\right) \\
&\quad + \cos\left(\frac{2z-h-t}{2t}\pi\right)\left(\theta_{\mathrm{wc}}+\frac{2y}{b}\theta_{\mathrm{wl}}\right)
\end{aligned}
\tag{1}
$$

The functions $\theta_{uc}(x)$, $\theta_{vc}(x)$, and $\theta_{wc}(x)$ describe the inhomogenous weak-layers centerline displacement of the weak layer, while $\theta_{ul}(x)$, $\theta_{vl}(x)$, and $\theta_{wl}(x)$ are the displacements at the free edges at the midplane

of the weak layer. From this displacement field, the strains and stresses for the weak layer can be computed and the strain energy is derived. The total internal energy is now given by the sum of slab and weak layers strain energy and dependent on the twelve unknown functions. 6 of those are derived from the slabs kinematics, while the other 6 are given in Equation 1.

Calculating the total potential energy in the supported slab requires now the external potential. This is linked to the work conducted on the supported slab. Work is conducted by gravitational forces on the slab and depends on the orientation of the specimen. Two rotational degrees of freedom are introduced. One is the inclination of the slab φ and denotes the angle between the x-axis and the horizontal plane. The other rotation is the tilt of the specimen about the x-axis. This tilt results in an out-of-plane bending deformation of the slab and is depicted in Figure 1.

The external work now computes to

$$-\Pi_{\text{ext}} = \mathcal{W}_{\text{ext}} = \sum_{i=1}^{N+1} \int_{z_{i-1}}^{z_i} \int_{-b/2}^{b/2} \rho_i \, g \begin{pmatrix} -\sin(\varphi) \\ \sin(\theta) \\ \cos(\varphi)\cos(\theta) \end{pmatrix} \cdot \begin{pmatrix} u(x,y,z) \\ v(x,y,z) \\ w(x,y,z) \end{pmatrix} \mathrm{d}y \, \mathrm{d}z. \tag{2}$$

The $N+1$st layer denotes the weak layer with its material properties. The total potential energy is now given as the sum of internal strain energy and the external potential, This potential is a functional of the 12 unknown functions u_0, v_0, w_0, ϕ_i with $i = x, y, z$ and θ_{jc} and θ_{jl} with $j = u, v, w$. The calculus of variations provides a tool for finding the minimum of this functional. The generated system of 12 second order ODEs is solved by standard means and results in 24 constants of integration.

2.3 Slabs without weak-layer support

The case of unsupported segments is tackled with Timoshenko beam theory. The kinematics from Figure 2 apply and the equations of equilibrium form a system of ODEs of second-order. The general solution for the unknown centerline displacements and rotations can be found by direct integration and results in 12 constants of integration.

2.4 Global solution and boundary conditions

The constants of integration are determined from boundary and transmission conditions. These allow to model infinite slabs or free ends. The case of PST and CPST specimen is tackled with free ends on both ends of the slab. The, from the cut already damaged, weak layer is considered by implementing a supported and unsupported slab. Between these two segments transmission conditions in form of the axial and vertical forces, bending and torsion moments, and continuous displacements are formulated. The stress-free state at the weak layers free surface is regarded by additional boundary conditions.

These transmission and boundary conditions form a system of linear equations. This system can be solved by any direct or iterative algorithm and is readily implemented in Python. For each bedded segment, 24 new degrees of freedom are added, while unbedded segments contribute 12 degrees of freedom. A CPST or PST specimen is reduced to 36 degrees of freedom and the solution is obtained in milliseconds.

Table 1: Mechanical properties of the slab. The single layers are numbered from top to bottom, so that layer 1 is the snow surface and layer 3 is closest to the weak layer. Young's modulus is calculated from the layer's density by the relation of Bergfeld et al. [2023].

Layer	Density [kg/m^3]	Young's modulus [MPa]	Thickness [cm]
1	180	5.03	12
2	270	29.93	12
3	350	93.77	12

3. MODEL VALIDATION

To validate the present model, the energy release rate for a typical profile of a generic slab is compared to finite element computations. The slab profile is given in Table 1. These values for the layering are used in the validation of other models (Weißgraeber and Rosendahl [2023]). The general properties of the PST for the validation specimen can be found in Table 2. Figure 1 shows an illustration of the CPST specimen. The finite element model is discretized with bi-quadratic 20–node continuum elements with reduced integration. The mesh is refined in the region of strong stress gradients, in particular the crack tips. In Figure 3 the energy release rate for a rotated PST specimen is given. Even though energy rates are slightly underestimated for the given profile, the present model generates a good approximation of the energy release rates for cross-slope propagation saw tests. Moreover, the analytical model is able to determine the contribution of different fracture modes. This allows one, to investigate the mixed-mode fracture envelope considering all three fracture modes, if sufficient experimental setups are provided.

A possible test for the determination is the CPST as proposed by Knoff [2014]. Below, this special test setup is investigated before a more sophisticated

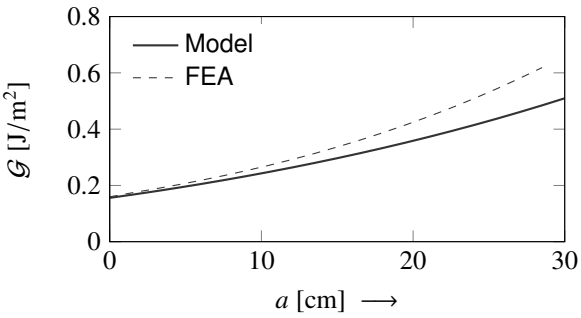

Figure 3: Energy release rate of cross-slope PST at $0°$ inclination and $38°$ rotation. The energy release rate of the FEA model is calculated using a central difference scheme from the total strain energies in the models with a partially collapsed weak layer.

Table 2: Properties of the validation specimen.

Property	Symbol	Value
Rotation	θ	$38\,°$
Inclination	φ	$0\,°$
Weak layer thickness	t	$2\,\mathrm{cm}$
Out-of-plane thickness	b	$30\,\mathrm{cm}$
Young's modulus weak layer	E^{wl}	$0.15\,\mathrm{MPa}$
Poisson ratio	ν	0.25
Length of PST block	l_{PST}	$250\,\mathrm{cm}$

experimental design is proposed.

4. MODE-MIXITY IN OF CROSS-SLOPE PROPAGATION SAW TESTS

Determining the mode III fracture toughness and the mode I–III fracture envelope demands for adequate experimental setups. Knoff [2014] proposed the cross-slope propagation saw test in order to reduce the effort of trench digging in extended field test campaigns. Using the present model for the test series conducted by Knoff [2014], the fracture toughness of the propagation saw tests could be determined. However, the missing slab properties in terms of densities and snow types result in large uncertainties of the calculated energy release rates. In order to get an insight into the contribution of different modes, some assumptions were made.

We used the mechanical properties from Table 1. The increasing snow density with increasing snow depth is seen in many snow profiles, so that this setup is deemed plausible. The layer thickness is adapted to the measured thickness by Knoff [2014], so that the slab is composed of three equally thick distinct layers. For very thick slabs, beam theory as applied in the kinematics of the present model does result in an inaccurate rendering of the displacements. Therefore, all experiments, where the slab's in-plane thickness h is larger than half the

Table 3: Experiments from Knoff [2014] taken into account in the present study. For the PST specimen the angle α corresponds to the inclination φ and for CPSTs to the tilt θ.

No.	α	h_{slab}	a_{PST}	a_{CPST}
1	$15\,°$	$45\,\mathrm{cm}$	$30\,\mathrm{cm}$	$24\,\mathrm{cm}$
2	$27\,°$	$28\,\mathrm{cm}$	$49\,\mathrm{cm}$	$38\,\mathrm{cm}$
3	$27\,°$	$42\,\mathrm{cm}$	$28\,\mathrm{cm}$	$25\,\mathrm{cm}$
4	$29\,°$	$45\,\mathrm{cm}$	$25\,\mathrm{cm}$	$25\,\mathrm{cm}$

Table 4: Fracture toughness and mode ratios for PST and CPST experiments from Table 3. The mode contributions are given as percentage of the calculated fracture toughness.

	$\mathcal{G}_{\mathrm{c}}^{\mathrm{PST}}$	$\frac{\mathcal{G}_{\mathrm{I}}}{\mathcal{G}_{\mathrm{c}}^{\mathrm{PST}}}$	$\frac{\mathcal{G}_{\mathrm{II}}}{\mathcal{G}_{\mathrm{c}}^{\mathrm{PST}}}$	$\frac{\mathcal{G}_{\mathrm{III}}}{\mathcal{G}_{\mathrm{c}}^{\mathrm{PST}}}$
1	$1.27\,\mathrm{J/m^2}$	$83\,\%$	$17\,\%$	$0\,\%$
2	$0.84\,\mathrm{J/m^2}$	$83\,\%$	$17\,\%$	$0\,\%$
3	$1.17\,\mathrm{J/m^2}$	$84\,\%$	$16\,\%$	$0\,\%$
4	$1.17\,\mathrm{J/m^2}$	$84\,\%$	$16\,\%$	$0\,\%$

	$\mathcal{G}_{\mathrm{c}}^{\mathrm{CPST}}$	$\frac{\mathcal{G}_{\mathrm{I}}}{\mathcal{G}_{\mathrm{c}}^{\mathrm{CPST}}}$	$\frac{\mathcal{G}_{\mathrm{II}}}{\mathcal{G}_{\mathrm{c}}^{\mathrm{CPST}}}$	$\frac{\mathcal{G}_{\mathrm{III}}}{\mathcal{G}_{\mathrm{c}}^{\mathrm{CPST}}}$
1	$0.64\,\mathrm{J/m^2}$	$76\,\%$	$16\,\%$	$8\,\%$
2	$0.70\,\mathrm{J/m^2}$	$72\,\%$	$16\,\%$	$12\,\%$
3	$0.71\,\mathrm{J/m^2}$	$65\,\%$	$14\,\%$	$21\,\%$
4	$0.86\,\mathrm{J/m^2}$	$63\,\%$	$14\,\%$	$22\,\%$

PST's length are dropped. Additionally, all tests with cut length of more than half the total block length are discarded. The remaining data points have angles between $15°$ and $29°$. The measured cut length and snow slab thickness for the tests are given in Table 3. The calculated energy release rates for both PST and CPST specimen are given in Table 4.

The PST results in terms of the fracture toughness align well with other test series (Bergfeld et al. [2023]). This indicates that the assumptions on the layering are plausible. The mode contribution of the singular fracture modes show that for all CPSTs the contribution of mode III is less than $25\,\%$.

While the measured crack length shows no significant dependence on the orientation of the PST, the actually measured fracture toughness does change significantly. That implies that crack propagation in mode III is subject to a lower fracture toughness $\mathcal{G}_{\mathrm{IIIc}}$ than crack propagation in mode I, $\mathcal{G}_{\mathrm{IIIc}} < \mathcal{G}_{\mathrm{Ic}}$. Thus, CPSTs can be used to identify the fracture toughness of weak layers subject to mode I–III mixity, but no direct information on the fracture toughness for pure mode III, $\mathcal{G}_{\mathrm{IIIc}}$ can be obtained. In order to increase the ratio of mode III and ideally determine the mode III fracture toughness from a pure mode III configuration, the results of Knoff [2014] are evaluated and a new test design is developed.

Table 5: Base configuration for the parameter study. The CPST blocks are considered to have a length of 250 cm.

Property	Value
Angle θ	55°
Out-of-plane width b	20 cm
Slab thickness h	36 cm
Cut length a	20 cm

5. MODE III FRACTURE TOUGHNESS TEST

From Table 4 some hypotheses on the influence of individual parameters can be derived. Larger tilt angles result in higher mode III contributions. Large cut lengths have the opposite effect and smaller cut lengths seem to result in higher mode III contributions. The slab's in-plane thickness seems to play an important role, as thicker slabs result in in higher mode III ratios. In order to validate these hypothesis, a parameter study is conducted. In addition to slab thickness, angle, and cut length, the slab's out-of-plane thickness is varied. These four parameters are varied independently from a base configuration. The base configuration is defined in Table 5.

The slab is again layered as given in Table 1 with the individual layer thicknesses scaled with the total slab thickness. In Figure 4, the results of these variations are given.

The results support some of the hypothesis derived from Table 4. Especially, an increasing tilt angle correlates with an increasing mode III contribution. For the cut length, a maximum in the mode III ratio can be found. For the slab thickness, an increase results in decreasing mode III contributions. An increasing out-of-plane thickness generally results in higher mode III contributions.

For the out-of-plane thickness b, the increase in mode III contributions can be explained mechanically. Increasing the thickness reduces the pure out-of-plane bending deformation as the slab becomes more squat, so that the out-of-plane shear deformations start to dominate. The out-of-plane bending results in a linear distribution of axial stresses σ_{xx} over the width of the slab. The tensile and compressive stresses at the edges result then in in-plane shear stresses in the weak layer. These create a mode II loading at the anticrack tip. Out-of-plane shear bending results in shear stresses τ_{xy} in the slab, which loads the anticrack tip with fracture mode III.

With increasing slab thickness b, mode II contributions decline and mode III increases. For in-plane bending and shearing, the slab thickness has a negligible effect, so that the absolute mode I values remain approximately constant.

For the design of a test, the following findings can be taken:

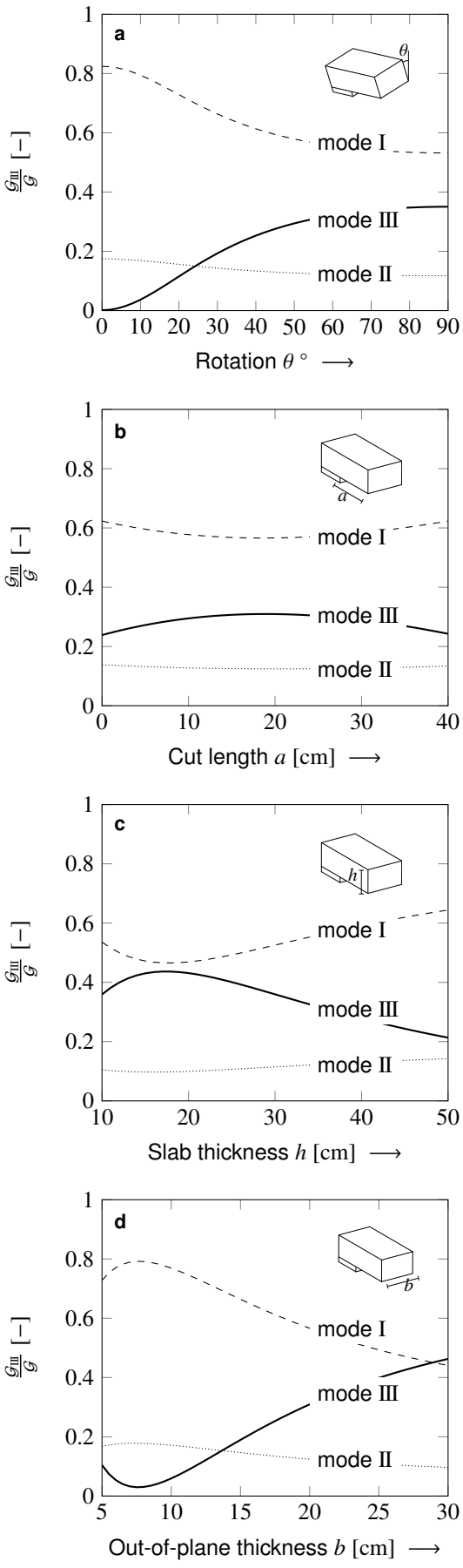

Figure 4: Mode contributions to the total energy release rate. Varied are the parameters denoted at the abscissa of the respective figure.

Figure 5: First mode III fracture toughness experiments on the Wannengrat, Davos (CH).

- Increase the tilt angle: Performing the experiments at a tilt angle of $90°$. Therefore, the PST is to be extracted from the snow pack and a tilting device similar to Adam et al. [2023] should be used.
- Increase the out-of-plane thickness: In general, larger out-of-plane thickness result in larger mode III contributions. However, for the experimental setup the thickness is limited by the weight that can be handled in the field.
- No general suggestions on the slab thickness and gut length can be made: In field experiments, these two properties are linked strongly, as thicker slabs result in higher loading and thus reduce the cut lengths for constant weak layer properties. In especially, we suggest thin slabs for ease of handling.

Especially the last point presents a critical problem, when reaching for high mode III tests in the field. A priori, the cut length is not known at a given slab thickness and weight, but influences the mode-ratio strongly. In order to be able to independently control slab thickness and loading, an advanced experimental setup is proposed in the next section.

6. EXPERIMENTAL SETUP FOR MODE III TEST ON WEAK LAYERS

Using a sled as proposed by Adam et al. [2023] provides one with the opportunity to transport and tilt snow slabs. Reducing the danger of collapsing the weak layer during the tilting requires additional precautions. For this purpose, the sled edges are designed high enough to support both weak layer and slab during the rotation. To be able to cut into the weak layer and prevent the substratum from out of plane bending, the whole specimen is pushed against a standing saw at the free end of the slab. This enables the support of the substratum by an additional steel plate to prevent the substratum from bending out-of-pane. At the point of the saw, the crack tip is loaded with out-of-plane bending. Additional weights can be placed at the upper side of the slab. A first implementation of this design is shown from a proof of concept at the Wannengrat test site located at Davos (CH) in Figure 5. Improvements from this setup are shown in Figure 6, where the possibility to additionally load the weak layer by weights is ensured by the asymmetric sled.

7. CONCLUSION

An analytical closed-form model is presented, which enables to evaluate mode III contributions from non-standard PSTs. The model provides stresses, displacements and energy release rates. It provides researchers with the opportunity to determine the fracture envelope for mixed mode I, II and III ratios. To this end, a test design for mode III tests is suggested, that can be used in the field to address the mode III fracture toughness of weak layers.

Additionally, an assessment of the conditions in cross-slope PSTs is provided. Our results show, that while the cut length remain unchanged under the different orientation of the PST, the fracture toughness does change significantly in the test design proposed by Knoff [2014].

The possibility to determine mode III fracture toughness of weak layers gives us the opportunity to measure a property that remained undetermined to the present and is very relevant for crack propagation in slopes leading to avalanche release.

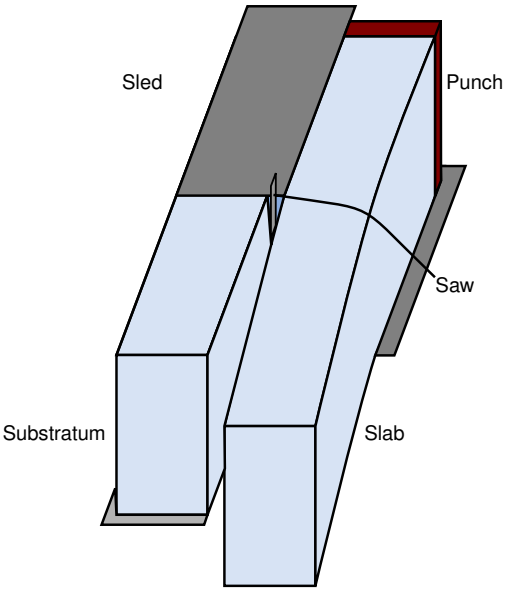

Figure 6: Design of experiment for mode III fracture toughness tests. The saw is fixated while the punch is pushed forward resulting in a damage to the weak layer between slab and substratum. By digging out a small trench under the unsupported slab prior to the experiment, the specimen is loaded with out-of-plane bending.

References

J. Schweizer, J. B. Jamieson, and M. Schneebeli. Snow avalanche formation. *Reviews of Geophysics*, 41(4), 2003. ISSN 8755-1209. doi: 10.1029/2002RG000123.

Joachim Heierli and Michael Zaiser. Failure initiation in snow stratifications containing weak layers: Nucleation of whumpfs and slab avalanches. *Cold Regions Science and Technology*, 52(3):385–400, 2008. ISSN 0165-232X. doi: 10.1016/j.coldregions.2007.02.007.

A. A. Griffith. Vi. the phenomena of rupture and flow in solids. *Philosophical Transactions of the Royal Society of London. Series A, Containing Papers of a Mathematical or Physical Character*, 221(582-593):163–198, 1921. ISSN 0264-3952. doi: 10.1098/rsta.1921.0006.

V. Adam, B. Bergfeld, F. Rheinschmidt, Walet, M. D. E. M., J. Schöttner, P. Weißgraeber, A. van Herwijnen, and P. L. Rosendahl. A field test for the mixed-mode fracture toughness of weak layers. In E. Peitzsch and S. Trautman, editors, *Proceedings fo the International Snow Science Workshop 2023*, Montana, 2023. Montana State University Libary.

P. Weißgraeber and P. L. Rosendahl. A closed-form model for layered snow slabs. *The Cryosphere*, 17(4):1475–1496, 2023. ISSN 1994-0416. doi: 10.5194/tc-17-1475-2023.

B. Trottet, R. Simenhois, G. Bobillier, B. Bergfeld, A. van Herwijnen, C. Jiang, and J. Gaume. Transition from sub-rayleigh anticrack to supershear crack propagation in snow avalanches. *Nature physics*, 18(9):1094–1098, 2022. ISSN 1745-2473. doi: 10.1038/s41567-022-01662-4.

E. Knoff. The pst with a twist: Comparing the standard pst to the cross slope pst. In P. Haegeli, editor, *Proceedings ISSW 2014. International Snow Science Workshop*, Montana, 2014. Montana State Universit Libary.

T. S. Methfessel and W. Becker. A generalized model for predicting stress distributions in thick adhesive joints using a high-order displacement approach: under review. *Coposite Structures*, 2022.

B. Gerling, H. Löwe, and A. van Herwijnen. Measuring the elastic modulus of snow. *Geophysical Research Letters*, 44(21), 2017. ISSN 0094-8276. doi: 10.1002/2017GL075110.

B. Bergfeld, A. van Herwijnen, G. Bobillier, P. L. Rosendahl, P. Weißgraeber, V. Adam, J. Dual, and J. Schweizer. Temporal evolution of crack propagation characteristics in a weak snowpack layer: conditions of crack arrest and sustained propagation. *Natural Hazards and Earth System Sciences*, 23(1):293–315, 2023. ISSN 1684-9981. doi: 10.5194/nhess-23-293-2023.